network beneath the epithelium from which IPCL in the epithelial papillae arose. IPCL were recognized as the terminal capillaries of the squamous epithelium, and then drained into the venules (Fig. 1c–e). Because these venules were thicker than arterioles, the arborescent vascular network that was evident using conventional endoscopy was considered to consist mainly of veins.

MICROVASCULAR ARCHITECTURE OF ESOPHAGEAL NEOPLASMS

Using ×120 magnifying endoscopy, Inoue *et al.* demonstrated that the IPCL of carcinoma in situ (M1) had characteristic changes such as 'dilatation, weaving, changes in caliber and variations in shape', compared with normal esophageal mucosa.[6] As cancer invaded the lamina propria mucosae (M2), the papillae became longer, and the IPCL revealed elongation as the tumor thickness increased (Fig. 2a–c).[7,14,16] However, there is some concern that the number of IPCL in a mucosal cancer increases in comparison with the normal squamous epithelium (Fig. 2d,e). Using CD105 antibody (endoglin), Kubota *et al.* counted the microvessel density (MVD) of lugol-unstained lesions with non-dysplastic epithelium (esophagitis), and low-grade and high-grade dysplasia of the squamous epithelium.[22] Endoglin/CD105 is well acknowledged as being the most reliable marker of endothelial cell proliferation, and is overexpressed on tumor vessels.[23] Kubota *et al.* mentioned that CD105-positive vessels were already present in esophagitis and low-grade dysplasia, and that CD105-positive MVD in high-grade dysplasia was significantly increased in comparison with low-grade dysplasia. These newly recruited capillaries are similar to adjacent modified IPCL in shape. However, in general, these capillaries may reveal hyper-permeability characteristics and have a fragile structure. We therefore, favour, the descriptive term 'intermixing of modified IPCL and immature IPCL-like capillaries (IPCL-like abnormal capillary)' for the vasculature of mucosal cancer (M1, M2) and dysplasia. Furthermore, the arborescent vascular network of M1 or M2 cancer that exists in the lamina propria mucosae and submucosa (beneath the tumor) is densely arranged in comparison with the normal squamous epithelium, based on stereoscopic microscopy observations after MICROFIL injection (Fig. 2f). In this connection, Kuwano *et al.* have reported that the MVD of M1 and M2 cancer determined on the basis of positivity for factor VIII-related antigen was significantly higher than that of adjacent normal squamous epithelium.[24] This phenomenon reflects the fact that, under magnifying endoscopic observations, the background mucosa without IPCL appears homogeneously reddish in comparison with normal squamous epithelium.

As cancer invades to the muscularis mucosae (M3), the tumor becomes thicker, and papillae begin to be destroyed. At the surface of the tumor, the newly developed vessels appear dilated and irregularly branched, with a shape that obviously differs in comparison with the IPCL-like capillaries of M1 or M2 cancer. When cancer has invaded to the submucosa (SM), the papillae are destroyed and the IPCL-like capillaries disappear completely. The newly developed vessels rearranged at the surface of the tumor (Fig. 2g–i)[6,7,14–16] are cancer specific and are not evident in benign lesions, except in special circumstances (e.g. after a biopsy procedure). Accordingly, we refer to these vessels as 'neovasculature'. As described above, the presence of neovasculature suggests that the depth of invasion must be greater than M3 and, therefore, this feature is a good indicator when considering the propriety of endoscopic mucosal resection.

MOLECULAR ANALYSIS OF ANGIOGENESIS DURING ESCC: CORRELATION WITH ENDOSCOPIC FINDINGS

The concept of a tumor angiogenesis factor that diffuses into the microenvironment and initiates the generation of tumor blood vessels was first proposed in 1971 by Folkman.[25,26] He considered that neovascularization is an event that separates the development of any solid tumor into two stages: (i) the avascular stage; and (ii) the vascular stage. In the avascular stage, nutrients and wastes are exchanged by simple diffusion from the host vessels. Capillary proliferation from the vascular system of the host can begin while the tumor colony is still very small. However, in the vascular stage, once capillaries have penetrated along the edge of a tumor, rapid exponential tumor growth begins. The morphological characteristics of tumor vessels have been described as tortuous, dilated, or irregular in shape.[27] Such vessels are also dead-ended and leaky. Because of these structural differences from normal vessels, the blood supply to tumors is often slow and may be intermittent.

Using the GIF-Y0002, we have been able to observe blood flow in the tumor vasculature in some cases.[14,15] Blood flow to mucosal cancer (modified IPCL with immature IPCL-like capillaries) seems to be maintained at a level similar to that provided by normal IPCL (Fig. 3a). In advanced cancer (with neovasculature), the surface vasculature is irregularly branched, and the blood flow is slow or often intermittent (Fig. 3b). The tumor vessels present at this point are consistent with those observed in M3 or deeper ESCC. Neovascularization is controlled and maintained by various angiogenic regulators produced by tumor and host cells.

Kitadai *et al.* have reported the molecular angiogenic profile of esophageal ESCC at the precancerous and cancerous stages. They carried out an immunohistochemical analysis of precancerous and cancerous lesions using antibodies against vascular endothelial growth factor (VEGF), platelet-derived endothelial cell growth factor/thymidine phosphorylase (PD-ECGF/TP), basic fibroblast growth factor (bFGF) and interleukin (IL)-8,[28] and observed initially enhanced expression of PD-ECGF/TP and VEGF in dysplastic lesions. bFGF and IL-8 were not expressed in dysplasias and mucosal carcinomas, but their expression increased in the late stage of cancer progression. Kitadai *et al.* concluded that angiogenic switching is a very early event in the development of ESCC. However, other reports have indicated that overexpression of VEGF is observed in cancer that has invaded beyond the submucosal layer.[29–32]

Similar to cyclooxygenase (COX)2, inducible nitric oxidase synthase (iNOS) is overexpressed in both mucosal and invasive esophageal cancer.[33–35] Production of these two enzymes occurs in chronically inflamed tissues, including precancerous lesions, and they are thought to have several functions. COX2 inhibits apoptosis and promotes angiogenesis,

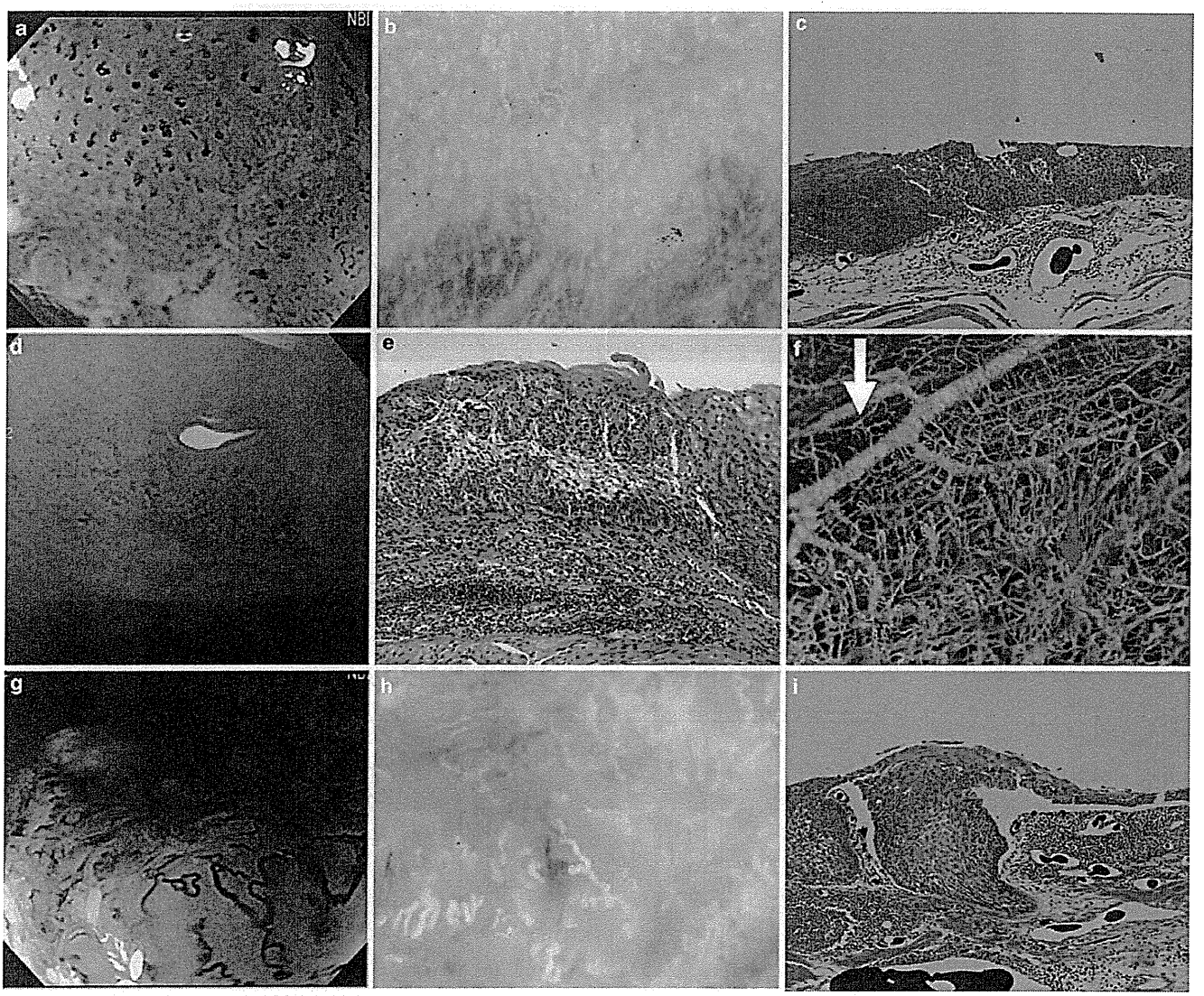

Fig. 2. (a) View of M2 cancer at ×80 magnification. Dilated and elongated intrapapillary capillary loops (IPCL) are evident. (b) Border between mucosal cancer and normal squamous epithelium after injection with MICROFIL (after iodine staining). The cancer lesion appears at the top. Arborescent vascular network is not evident in the area of the cancer. IPCL in the cancer lesion show characteristic changes, such as dilation, weaving, and alterations of shape in comparison with the normal epithelium. (This figure is quoted from ref. no. 17.) (c) Histological view of the same section as that in Fig. 2b. The depth of invasion is considered to be M1. (d) Observation of a tiny esophageal cancer at ×80 magnification. IPCL-like vessels are densely arranged in comparison with the adjacent normal esophageal mucosa. (This figure is quoted from ref no. 48.) (e) Histological view of the cancer lesion shown in Fig. 2d. Densely arranged micro-capillaries are evident. These capillaries are not present in the epithelial papillae. (This figure is quoted from ref. no. 48.) (f) Border between normal esophageal mucosa and mucosal cancer revealed by stereoscopic microscopy after injection of MICROFIL (after methyl-salicylate penetration procedure). White arrow indicates the position of the normal epithelium, and the dense aborescent vascular network is highlighted with a red arrow. (g) Submucosal cancer at ×80 magnification. The neovasculature shows obvious dilation and irregular branching (narrow band imaging). (h) Area of M3 invasion after MICROFIL injection, showing irregularly branched neovasculature. (This figure is quoted from ref. no.7.) (i) Histological section of Fig. 2h. The depth of invasion is considered to be M3. (This figure is quoted from ref. no. 7.)

whereas iNOS is also involved in various stages of neovascularization from vasodilatation to vascular remodeling.[36]

Hypoxia-inducible factor (HIF-1) is recognized as an important protein that regulates transcription of several genes related to angiogenesis, including VEGF, plasminogen activator inhibitor-1 and VEGF receptor-1. In the ESCC, HIF-1-alpha is overexpressed in submucosal cancer;[37,38] however, examination concerning mucosal cancer is undetermined.

Several oncogenes and tumor-suppressor genes, including *HER2* and *p53*, play a significant role in promoting or suppressing neovascularization.[39–42] For example, abnormalities of *p53* are thought to facilitate neovascularization by downregulating the production of TSP-1 (a potent negative

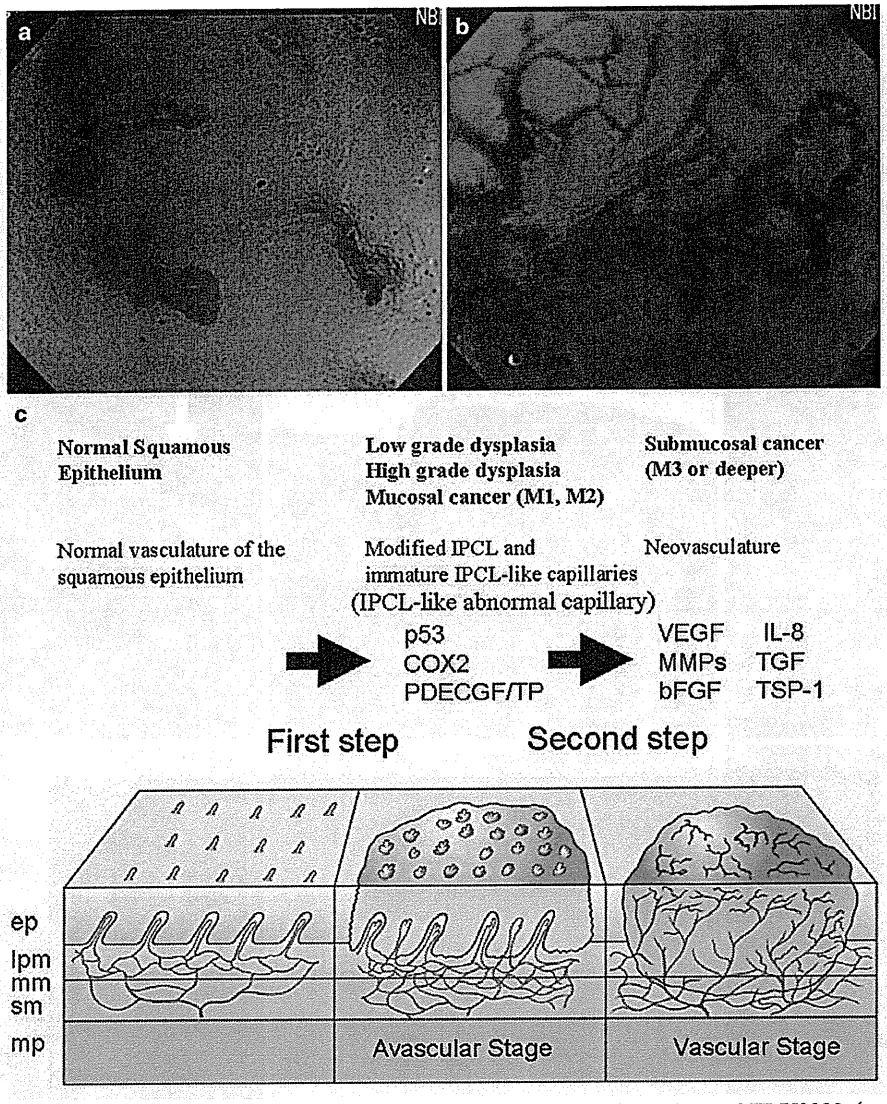

Fig. 3. (a) Microvasculature of M2 esophageal cancer at the highest magnification of the GIF-Y0002 (narrow band imaging). Dilated intrapapillary capillary loops (IPCL) compared with normal IPCL and moving blood cells inside the tumor vasculature can be seen. In this case, the speed of the blood flow is maintained in the superficial lesions in comparison with the normal vasculature. (b) Microvasculature of advanced esophageal cancer at the highest magnification of the Y0002 (narrow band imaging). Significantly dilated neovasculature of the advanced tumor can be seen. In this case, the blood flow inside the vasculature was significantly slow. The shape of the red blood cells is also recognizable. (c) Hypothesis of 'multi-step angiogenesis' in the early stage of esophageal squamous cell carcinoma (ESCC). ep, epithelium; lpm, lamina propria mucosae; mm, muscularis mucosae; mp, muscularis propria; sm, submucosa. (This figure is partially quoted from ref. no. 15.)

endothelial regulator).[42] In ESCC, *p53* mutations have been detected at all stages of carcinogenesis, from precancerous lesions, such as hyperplasia or dysplasia, to invasive cancer.[39] However, thrombospondin (TSP)-1 is overexpressed at the late stage of cancer progression.[43]

Transforming growth factor-alpha (TGF-α), known to be an endothelial mitogen and angiogenesis inducer of VEGF expression, is not expressed in cancer in situ, but is overexpressed in T1 cancer.[29]

Various metalloproteinases (MMP) and other proteases, such as trypsin, are involved in neovascularization and tumor-induced proteolysis. These enzymes tend to be expressed at higher levels in tumors that have invaded to the submucosa or deeper.[44–46]

Considering these findings as a whole, it seems that the initial angiogenic switch occurs at the precancerous stage or in mucosal cancer. However, at this stage, as the vascularity is present mainly in the lamina propria mucosae or epithelial papillae and has not yet penetrated the tumor, we should consider this to be the 'avascular' stage. In addition, at this stage, the morphology of the surface vasculature is similar to that of the vasculature of the inflammation from the magnifying endoscopic findings at the point of dilation and elongation of the IPCL, with recruitment of the IPCL-like immature capillaries. Various endothelial regulators do not become upregulated during localized cancer growth in the mucosal layer, but their production increases as the cancer invades the submucosa or deeper layer. From the magnifying endoscopic

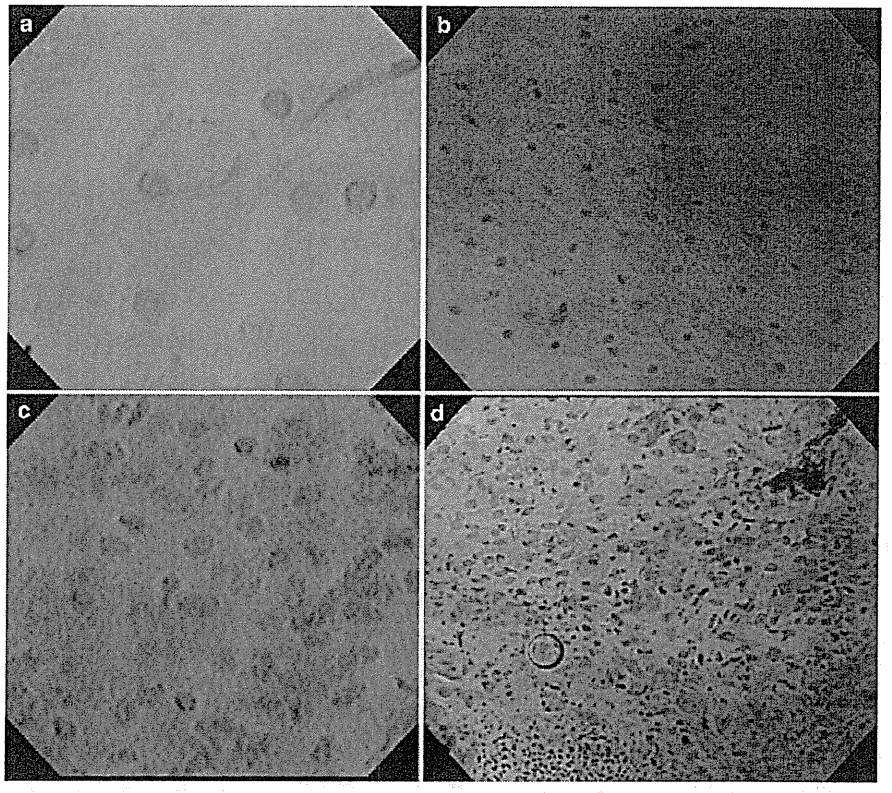

Fig. 4. (a) Normal squamous epithelial cells observed with the XEC120U (Olympus Medical Systems Co., Tokyo, Japan) (×1125, methylene blue staining). Homogeneous and blue squamous epithelial cells are evident. The nuclear-cytoplasmic ratio is uniform and low. (b) Normal squamous epithelial cells observed with the GIF-Y0002 (×380, methylene blue staining). One or two layers of the surface squamous epithelial cells can be seen at lower magnification, in comparison with the XEC120U. (c) Esophageal squamous cell carcinoma at ×1125 magnification. Nuclear density is higher and nuclear abnormalities are evident (methylene blue staining). (d) Esophageal squamous cell carcinoma observed with the GIF-Y0002 (methylene blue staining). A marked increase in nuclear density and nuclear abnormality is evident.

observation, neovasculature could be observed when the cancer invades into the muscularis mucosa (M3). It is at this stage that growth of the tumor vasculature starts to become apparent ('vascular' stage). A second angiogenic step exists in ESCC when the cancer invades the muscularis mucosa (Fig. 3c). However, the mechanism of formation of the neovasculature is still unclear. Further investigation is necessary.

FUTURE APPLICATIONS OF MAGNIFYING ENDOSCOPY FOR ESCC: ENDOCYTOSCOPIC HISTOLOGICAL DIAGNOSIS

Microvasculature can be formed secondarily as a result of histological abnormalities, such as esophagitis, dysplasia or ESCC; biopsy histology cannot be omitted only on the basis of microvascular architecture. In order to conclude whether target mucosa reveals malignancy, observation of nuclear abnormality is necessary using biopsy histology or other methods.

In 2003, Olympus Medical Systems Corporation introduced a probe-type endocytoscopy system (ECS). ECS is based on the technology of light-contact microscopy. The most evident use of ECS is for real-time, high-resolution diagnosis of nuclear abnormalities (Fig. 4). Kumagai *et al.* were the first to report *in vivo* observations of squamous epithelium and ESCC using ECS,[14,15,47,48] and proposed a classification of the esophageal mucosa based on a flow chart of features observed using this system. They also worked in consultation with a pathologist to evaluate whether ECS observation might be able to replace biopsy histology. It was concluded that ECS would be able to replace histological examination of biopsy samples in approximately 84% of ESCC if a magnification of ×1125 was used, considering that an increase of nuclear density and nuclear abnormalities would be sufficiently convincing proof of malignancy.[47]

From this viewpoint, endocytoscopic histological diagnosis and endoscopic therapy may be carried out simultaneously in a limited area of squamous mucosa. However, histological examination of EMR and ESD specimens remains very important for estimating the tumor-free resection margin, lymph node metastasis and patient outcome.[49] GIF-Y0002 can visualize the surface cells, and is an excellent ECS instrument in terms of ease of use, ready access to lesions, and durability of the endoscope, and we consider that ECS has potential for screening use. It is anticipated that, eventually, the power of the magnifying endoscope will be improved to allow observations at the cellular level, thus dispensing with the need for biopsy histology.

REFERENCES

1. The Japan Esophageal Society. Japanese Classification of esophageal cancer, tenth edition: part 1. *Esophagus* 2009; **6**: 1–25.
2. Kuwano H, Nishimura Y, Ohtu A *et al.* Guidelines for diagnosis and treatment of carcinoma of the esophagus April 2007 edition: part1 Edited by the Japan esophageal society. *Esophagus* 2008; **5**: 61–73.
3. Kuwano H, Nishimura Y, Ohtu A *et al.* Guidelines for diagnosis and treatment of carcinoma of the esophagus April 2007 edition: part2 Edited by the Japan esophageal society. *Esophagus* 2008; **5**: 117–32.

4. Ozawa S, Tachimori Y, Baba H *et al.* Comprehensive registry of esophageal cancer in Japan, 2001. *Esophagus* 2009; **6**: 95–110.
5. Inoue H, Honda T, Yoshida T *et al.* Ultra-high magnification endoscopy of the normal esophageal mucosa. *Dig. Endosc.* 1996; **2**: 134–8.
6. Inoue H, Honda T, Nagai K *et al.* Ultra-high magnification endoscopic observation of carcinoma in situ. *Dig. Endosc.* 1997; **1**: 16–18.
7. Kumagai Y, Inoue H, Nagai K, Kawano T, Iwai T. Magnifying endoscopy, stereoscopic microscopy and the microvascular architecture superficial esophageal carcinoma. *Endoscopy* 2002; **34**: 369–75.
8. Muto M, Horimatsu T, Ezoe Y, Morita S, Miyamoto S. Improving visualization techniques by narrow band imaging and magnification endoscopy. *J. Gastroenterol. Hepatol.* 2009; **24**: 1333–46.
9. Kumagai Y, Toi M, Inoue H. Dynamism of tumour vasculature in the early phase of cancer progression: Outcomes from oesophageal cancer research. *Lancet Oncol.* 2002; **3**: 604–10.
10. Kozu T, Takahashi H, Kuga K *et al.* Microscopic observation of esophageal mucosa using a magnifying endoscope. *Gastroenterol. Endosc.* 1975; **17**: 810–17 (in Japanese with English Abstract).
11. Makuuchi H, Machimura T, Sou Y *et al.* Examination of esophageal superficial cancer by magnifying endoscopy. *Endoscopia Digestiva* 1991; **3**: 412–21 (in Japanese with English Abstract).
12. Arima M, Tada M, Arima H. Evaluation of microvascular patterns of superficial esophageal cancers by magnifying endoscopy. *Esophagus* 2005; **2**: 191–7.
13. Arima M, Arima H, Tada M, Tanaka Y. Diagnostic accuracy of tumor staging and treatment outcomes in patients with superficial esophageal cancer. *Esophagus* 2007; **4**: 145–53.
14. Kumagai Y, Kawada K, Yamazaki S *et al.* Endocytoscopic observation of esophageal squamous cell carcinoma. *Dig. Endosc.* 2010; **22**: 10–16.
15. Kumagai Y, Kawada K, Yamazaki S *et al.* Prospective replacement of magnifying endoscopy by a newly developed endocytoscope, the 'GIF-Y0002'. *Dis. Esophagus* 2010; (in press).
16. Kumagai Y, Iida M, Yamazaki S. Magnifying endoscopic observation of the upper gastrointestinal tract. *Dig. Endosc.* 2006; **18**: 165–72.
17. Kumagai Y, Inoue H, Kawano T. Magnifying endoscopic observation of superficial esophageal carcinoma. *Dig. Endosc.* 2004; **16**: 277–81.
18. Kegaries D. The venous plexus of the oesophagus: Its clinical significance. *Surg. Gynecol. Obstet.* 1934; **58**: 46–51.
19. Butler H. The veins of the oesophagus. *Thorax* 1951; **6**: 276–96.
20. DeCarvalho CAF. Sur l'angio- architecture veineuse de la zone de transition oesophago-gastrique et son interpretation fonctionnelle. *Acta Anat.* 1966; **64**: 125–62.
21. Aharinejad S, Lametschwandtner A, Franz P *et al.* The vascularization of the digestive tract studied by scanning electron microscopy with special emphasis on the teeth, esophagus, stomach, small and large intestine, pancreas, and liver. *Scanning Microsc.* 1991; **5**: 811–49.
22. Kubota Y, Kaneko K, Konishi K *et al.* The onset of angiogenesis in a multistep process of esophageal squamous cell carcinoma. *Front. Biosci.* 2009; **14**: 3872–8.
23. Li SL, Gao DL, Zhao ZH *et al.* Correlation of matrix metalloproteinase suppressor genes RECK, VEGF, and CD105 with angiogenesis and biological behavior in esophageal squamous cell carcinoma. *World J. Gastroenterol.* 2007; **13**: 6076–81.
24. Kuwano H, Sonoda K, Yasuda M *et al.* Tumor invasion and angiogenesis in early esophageal squamous cell carcinoma. *J. Surg. Oncol.* 1997; **65**: 188–93.
25. Folkman J. Proceedings: Tumor angiogenesis factor. *Cancer Res.* 1974; **34**: 2109–13.
26. Folkman J. Tumor angiogenesis. *Adv. Cancer Res.* 1974; **19**: 331–58.
27. Bergers G, Benjamin LE. Tumorigenesis and the angiogenic switch. *Nat. Rev. Cancer* 2003; **3**: 401–10.
28. Kitadai Y, Onogawa S, Kuwai T *et al.* Angiogenic switch occurs during the precancerous stage of human esophageal squamous cell carcinoma. *Oncol. Rep.* 2004; **11**: 315–19.
29. Li Z, Shimada Y, Uchida S *et al.* TGF-alpha as well as VEGF, PD-ECGF and bFGF contribute to angiogenesis of esophageal squamous cell carcinoma. *Int. J. Oncol.* 2000; **17**: 453–60.
30. Ogata Y, Harada Y, Fujii T, Yamana H, Fujita H, Shirouzu K. Immunohistochemical localization of vascular endothelial growth factor in esophageal cancer. *Kurume Med. J.* 1996; **43**: 157–63.
31. Uchida S, Shimada Y, Watanabe G *et al.* In oesophageal squamous cell carcinoma vascular endothelial growth factor is associated with p53 mutation, advanced stage and poor prognosis. *Br. J. Cancer* 1998; **77**: 1704–9.
32. Arii S, Mori A, Uchida S, Fujimoto K, Shimada Y, Imamura M. Implication of vascular endothelial growth factor in the development and metastasis of human cancers. *Hum. Cell* 1999; **12**: 25–30. Review.
33. Shamma A, Yamamoto H, Doki Y *et al.* Up-regulation of cyclooxygenase-2 in squamous carcinogenesis of the esophagus. *Clin. Cancer Res.* 2000; **6**: 1229–38.
34. Zimmermann KC, Sarbia M, Weber AA, Borchard F, Gabbert HE, Schror K. Cyclooxygenase-2 expression in human esophageal carcinoma. *Cancer Res.* 1999; **59**: 198–204.
35. Tanaka H, Kijima H, Tokunaga T *et al.* Frequent expression of inducible nitric oxide synthase in esophageal squamous cell carcinomas. *Int. J. Oncol.* 1999; **14**: 1069–73.
36. Chiarugi V, Magnelli L, Gallo O. Cox-2, iNOS and p53 as play-makers of tumor angiogenesis (review). *Int. J. Mol. Med.* 1998; **2**: 715–19.
37. Ogane N, Yasuda M, Shimizu M *et al.* Clinicopathological implications of expressions of hypoxia-related molecules in esophageal superficial squamous cell carcinoma. *Ann. Diagn. Pathol.* 2010; **14**: 23–9.
38. Kimura S, Kitadai Y, Kuwai T *et al.* Expression of p53 protein in esophageal squamous cell carcinoma: Relation to hypoxia-inducible factor-1alpha, angiogenesis and apoptosis. *Pathobiology* 2005; **72**: 179–85.
39. Bennett WP, Hollstein MC, Metcalf RA *et al.* p53 mutation and protein accumulation during multistage human esophageal carcinogenesis. *Cancer Res.* 1992; **52**: 6092–7.
40. Biramijamal F, Allameh A, Mirbod P, Groene HJ, Koomagi R, Hollstein M. Unusual profile and high prevalence of p53 mutations in esophageal squamous cell carcinomas from northern Iran. *Cancer Res.* 2001; **61**: 3119–23.
41. Tanaka S, Mori M, Akiyoshi T *et al.* Coexpression of Grb7 with epidermal growth factor receptor or Her2/erbB2 in human advanced esophageal carcinoma. *Cancer Res.* 1997; **57**: 28–31.
42. Dameron KM, Volpert OV, Tainsky MA, Bouck N. Control of angiogenesis in fibroblasts by p53 regulation of thrombospondin-1. *Science* 1994; **265**: 1582–4.
43. Oshiba G, Kijima H, Himeno S *et al.* Stromal thrombospondin-1 expression is correlated with progression of esophageal squamous cell carcinomas. *Anticancer Res.* 1999; **19**: 4375–8.
44. Sato F, Shimada Y, Watanabe G, Uchida S, Makino T, Imamura M. Expression of vascular endothelial growth

factor, matrix metalloproteinase-9 and E-cadherin in the process of lymph node metastasis in oesophageal cancer. *Br. J. Cancer* 1999; **80**: 1366–72.
45. Yamashita K, Mori M, Kataoka A, Inoue H, Sugimachi K. The clinical significance of MMP-1 expression in oesophageal carcinoma. *Br. J. Cancer* 2001; **84**: 276–82.
46. Ohashi K, Nemoto T, Nakamura K, Nemori R. Increased expression of matrix metalloproteinase 7 and 9 and membrane type 1-matrix metalloproteinase in esophageal squamous cell carcinomas. *Cancer* 2000; **88**: 2201–9.
47. Kumagai Y, Monma K, Kawada K. Magnifying chromoendoscopy of the esophagus: In-vivo pathological diagnosis using an endocytoscopy system. *Endoscopy* 2004; **36**: 590–4.
48. Kumagai Y, Takubo K, Iida M, Yamazaki S, Kawano T. A tiny esophageal cancer which was accurately diagnosed by magnifying endoscopy and endo-cytoscopy system. Report of a case. *Esophagus* 2007; **4**: 173–6.
49. Early squamous cell carcinoma of the oesophagus: The Japanese viewpoint. Takubo K, Aida J, Sawabe M *et al. Histopathology* 2007; **51**: 733–42. Review.

10.1109/ULTSYM.2010.0540

Adaptive Depth Compensation Algorithm for Photoacoustic Tomography

Shuhui Bu*, Makoto Yamakawa†, and Tsuyoshi Shiina*
*Graduate School of Medicine, Kyoto University, Kyoto, Japan
†Advanced Biomedical Engineering Research Unit, Kyoto University, Kyoto, Japan

Abstract—**Photoacoustic (PA) tomography is a rapidly developing imaging modality that provides high-contrast, high spatial-resolution images for vessel distributions in tissue. It can be applied to early breast cancer detection, and therefore it will be a valuable method for breast cancer diagnosis. Tissue absorbs and scatters light, and the optical fluence is known to approximately decrease exponentially. The pixels or voxels in a reconstructed PA image represent the level of absorbed optical energy, which is the product of the absorption coefficient and the optical fluence. Therefore, the contrast of tumors in deep tissue decreases because the optical fluence is low. Quantitative photoacoustic image reconstruction has been proposed to resolve this problem, but the process is based on compensating the reconstructed image with a pre-calculated optical fluence distribution. Because the contrast-to-noise-ratio (CNR) in the reconstructed images of deep tissue is low, amplification also magnifies the noise, which decreases the image quality. Here we propose a novel adaptive depth attenuation compensation algorithm that can provide greater imaging depth without degrading the CNR. The proposed method is evaluated by numerical simulation and a phantom experiment. The results of simulation and the phantom experiment indicate that the proposed method performs better than conventional methods.**

I. Introduction

The PA effect [1], [2] refers to the generation of acoustic wave by the absorption of electromagnetic (EM) energy including optical and radio-frequency wave. In PA tomography (PAT), sounds or stress waves are produced by illuminating the target with a short-pulse laser because of the thermoelastic expansion. Acoustic sensors are placed at surrounding positions, and the PA signals are recorded. The absorption source can be recovered through the reconstruction algorithm. Because the delivered energy type is light, the scattering of ultrasound echo imaging can be avoided. PAT combines the advantages of optical and acoustic methods: sensitive optical absorption contrast and low acoustic scattering in soft tissue. PAT has much better spatial resolution at depths exceeding the optical ballistic regime than the traditional optical modalities. In tissue, where the hemoglobin molecule of blood is the primary absorber, knowledge of the absorbed optical energy distribution can provide the local structure of blood circulation. In the early stage of cancer, the capillary vessel density will be increased. Based on this fact, cancer, especially breast cancer, can be detected by PAT before other image modalities can be image it.

One major problem in PAT is that the reconstructed information is not quantitative. Tissue absorbs and scatters light, so the optical fluence decreases with light penetration depth. The pixels or voxels in reconstructed PAT images represent the level of absorbed optical energy, which is the product of the absorption coefficient and the optical fluence. Therefore, the CNR in the deeper region of reconstructed images is low. A quantitative reconstruction method [3] has been proposed to resolve this problem, but the process is based on compensating the reconstructed image by a pre-calculated optical fluence distribution. Because the CNR in reconstructed images of deep tissue is low, amplification also magnifies the noise, which decreases the image quality.

In this paper, we introduce a novel adaptive depth attenuation-compensation algorithm that can partly overcome the above drawback. In the first step of this method, the PA signals are adaptively amplified. Next, the initially guessed absorption coefficients are reconstructed by the universal back-projection (UBP) method [4], [5]. Finally, an iterative algorithm [6]–[8] is applied to ensure proper compensation for achieving quantitative reconstruction. The advantage of the proposed method is that there is less noise in deep regions, This method also has the advantages of iterative reconstruction. The results of simulation and a phantom experiment indicate that the proposed method performs better than conventional methods.

The rest of this paper is organized as follows. In section II, we present the principle of the proposed method. Numerical simulation and a phantom experiment are described in section III. Finally, the conclusions of our work are provided in section IV.

II. Method

The proposed method is composed of two major stages. In the first stage, the detected PA signals are pre-amplified to increase the SNR in the deep region. In the second stage, an iterative reconstruction method is used to correct the improper depth compensation. The processing flow is illustrated in Fig. 1.

In the first stage, the first step is detecting the position and range of the target in the received PA signals. The processing is illustrated in Fig. 2. The envelop of detected PA signals is achieved by low-pass-filtering and Hilbert transformation. The peaks of the envelop signal are estimated, and only peaks with amplitudes exceeding a given threshold are selected. Next, the detected PA signals are amplified only at the selected peaks' positions, and the amplification coefficient is determined by taking the reciprocal of the pre-calculated optical

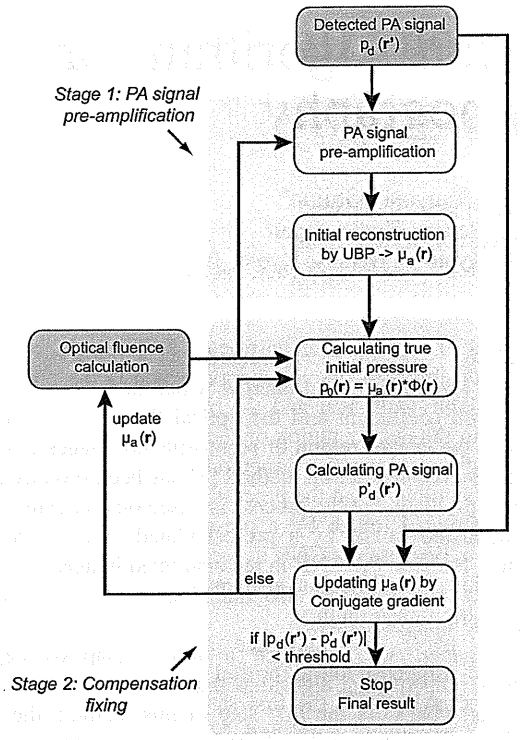

Fig. 1. Processing flow chart of proposed depth compensation algorithm for PAT. The processing contains two major stages: PA signal pre-amplification and compensation fixing.

fluence calculated from a Monte Carlo model. Because the PA signals are compensated by the reciprocal of optical fluence, the reconstructed value represents the absorption distribution. In this research, the initially guessed absorption distribution $\mu_a(\mathbf{r})$ is reconstructed by the UBP method.

Obviously, the initially guessed absorption distribution may not be correct. In order to correct the compensation, an iterative reconstruction method is utilized in the second stage. In this method, we define the update value in each iteration as the absorption coefficient. The initial pressure $p_0(\mathbf{r})$ is required to compare the detected PA signal and the PA signal calculated by the forward model. The initial pressure is defined as:

$$p_0(\mathbf{r}) = \Gamma\Phi(\mathbf{r})\mu_a(\mathbf{r}), \tag{1}$$

where Γ is the Grüenisen coefficient expressed as $\Gamma = \beta c^2/C_p$. Here we assume the Grüenisen coefficient is constant in the region of interest (ROI). Therefore, the forward model can be expressed as:

$$\mathbf{p} = \mathbf{A}\Phi\boldsymbol{\mu}_a, \tag{2}$$

where $\mathbf{A}$ denotes the system matrix that represents the geometric relationship between the initial pressure and the detected PA signal. The detailed definition of $\mathbf{A}$ is:

$$A_{i,j} = \frac{A^{vp}_{i,j+1} - A^{vp}_{i,j-1}}{2\Delta t}, \tag{3}$$

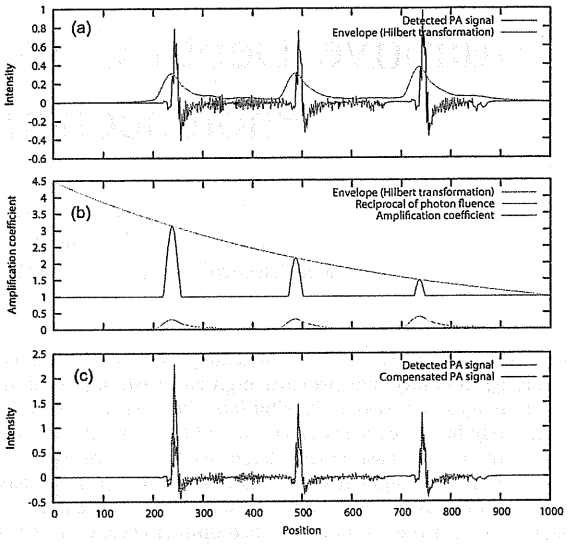

Fig. 2. Illustration of PA signal pre-amplification. (a) Detected PA signal and its envelop. (b) Reciprocal of pre-calculated optical fluence and amplification coefficient. (c) Detected PA signal and compensated PA signal.

where Δt is the time interval between two sampling points, and $A^{vp}_{i,j}$ represents the velocity potential. In the 3-D planar scanning environment, the voxel is usually much larger than the distance between two sampling point. Therefore, the calculated velocity potentials are not continuous, and after the finite-difference calculation, a large amplitude fluctuation will occur that prevents high-accuracy forward modeling. In this research, a Gaussian function is applied to interpolate the velocity potential data. The interpolated velocity potential is defined as:

$$\begin{aligned} A^{vp}_{i,j} &= \frac{\beta}{4\pi C_p}\frac{h_{i,j}}{R_{i,j}}, \\ R_{i,j} &= |\mathbf{r}_i - \mathbf{r}_j|, \\ h_{i,j} &= \begin{cases} \exp\left(\frac{-2(R_{i,j}-t_j v_s)^2}{\Delta^2}\right) : if|t_j - \frac{R_{i,j}}{v_s}| < \Delta/v_s, \\ 0 : else \end{cases} \end{aligned} \tag{4}$$

where Δ is the distance between the central point of adjacent voxels, C_p is the isobaric specific heat, β is the isobaric volume expansion coefficient, and v_s is the acoustic speed.

After interpolation, accurate forward modeling can be achieved, but matrix $\mathbf{A}$ is very large, which prevents implementation. Matrix $\mathbf{A}$ is a sparse matrix in which almost 99.5% of the entries are zero. Using the compressed sparse row (CSR) format [9] can greatly reduce the required memory. In the CSR format, only column indices and nonzero values and indices are stored. In the PAT mode, the ultrasound sensor assumed that it can receive pressure waves from the directions of $0 \sim 90$ degrees with the same sensitivity. In reality situation, however, the sensitivity is not uniform. To reduce the matrix size, the data outside a limited angles are ignored. Based on this fact, matrix $\mathbf{A}$ can be further decreased to about half.

The quantitative depth compensated absorption coefficient is estimated by minimizing l_2 norm between detected signals

TABLE I
SIMULATION PARAMETERS

Parameter Name	Value
Sound speed	1500 m/s
Sampling frequency	20 MHz
Sampling point number	750
Sensor number in x and y axes	16
Sensor pitch in x and y axes	2.0 mm
Voxel number in x, y, and z axes	64
Voxel size in x, y, and z axes	0.5 mm

and the PA signals calculated by the forward model, as shown below

$$\mu_a' = \arg\min_{\mu_a} ||\mathbf{p_d} - \mathbf{A}\Phi\mu_a||_2. \quad (5)$$

Here, $\mathbf{p_d}$ is the detected PA signal, and μ_a' is the optimal estimated absorption coefficient. The conjugate gradient method [10] is used to find the optimal estimate.

III. Simulation and Phantom Experiment

The proposed method was evaluated by numerically simulating a hypothetical model, as illustrated in Figs. 3(a)-(c). In this model, three pencil leads are simulated. The background's absorption coefficient is $\mu_a = 0.048$ cm^{-1}, and the scattering coefficient is $\mu_s = 100$ cm^{-1}. The PA waves are simulated by the k-space method [11], and -20 dB of white noise is added. The simulation parameters are summarized in Table I. After the simulated PA signal is obtained, a parallel implemented program is used to reconstruct the absorption coefficient. The resulting maximum intensity projection (MIP) images generated by UBP and pixel compensation are presented in Figs. 3(d)-(f). The resulting images of the proposed method are presented in Figs. 3(g)-(i). From the images, we can see that there are many side lobes and artifacts in the images reconstructed by the UBP method. In contrast, using the proposed method greatly decreases the side lobes and artifacts. In addition, the target in the images generated by UBP is larger than the actual size, while the target size in images generated by the proposed method is the same as the actual size.

In the phantom experiment, a Q-switched Nd:YAG laser at 1064 nm is used to illuminate the object. The laser has a PRF of 10 Hz and pulse duration of 10 ns. A 2 mm diameter hydrophone performs a 2-D plan raster scan to acquire PA signals. The PA signals are digitalized at 25 MHz and then stored in a computer. Targets are composed of 0.5 mm diameter pencil lead segments. The surrounding material is composed of gelatine mixed with 1% intralipid. These optical properties are close to those of tissue such as breast and skin. There are 33 raster scans for the x axis and 30 for the y axis. The pitch is 2 mm, and the ranges of reconstruction are 66 mm for the x axis, 60 mm for the y axis, and 50 mm for the z axis. The voxel size is 0.5 mm for all axes. The resulting images are presented in Fig. 4. The MIP images generated by the UBP method without depth compensation are displayed in Figs. 4(a)-(c). The MIP images generated by the UBP method with conventional depth compensation are displayed in Figs. 4(d)-(f). The MIP images generated by the proposed method are presented in Figs. 4(g)-(i). In the second stage, matrix $\mathbf{A}$ will consume 37 G byte of memory, which exceeds the current used computer's memory size. As a result, images are generated only by the first stage of the proposed method. Although there is no quantitative fixing step, the resulting images are also promising. The artifacts are greatly decreased compared with images generated by the conventional depth-compensation method.

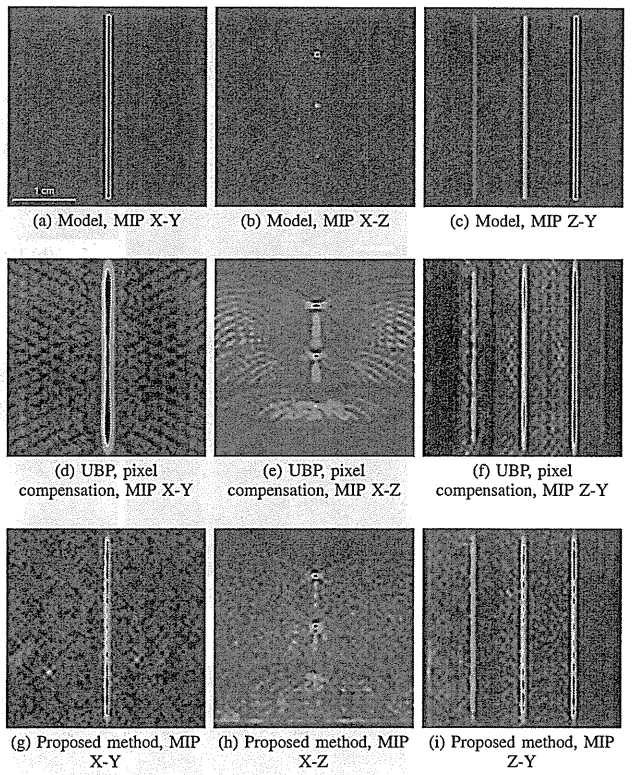

Fig. 3. Reconstructed images by UBP method and proposed method. MIP X-Y is projection along z axis, MIP X-Z is project along y axis, and MIP Z-Y is projection along x axis. (a)-(c) Simulation model. (d)-(f) Reconstructed images by UBP and conventional depth compensation method. (g)-(i) Reconstructed by proposed method.

Although the proposed method can output better quality images with fewer artifacts, two major problems need to be resolved before practical application. First, the proposed method requires a huge memory and much calculation time. Compressed sensing reconstruction, which can reduce the measurement data, will help to reduce the memory requirement. The calculation could potentially be performed by high-performance parallel computation. Therefore, in subsequent research, we will investigate a GPU-accelerated compressed-sensing reconstruction method. Second, iterative reconstruction is more sensitive to noise than other methods such as UBP. A more effective denoising method will therefore also be investigated.

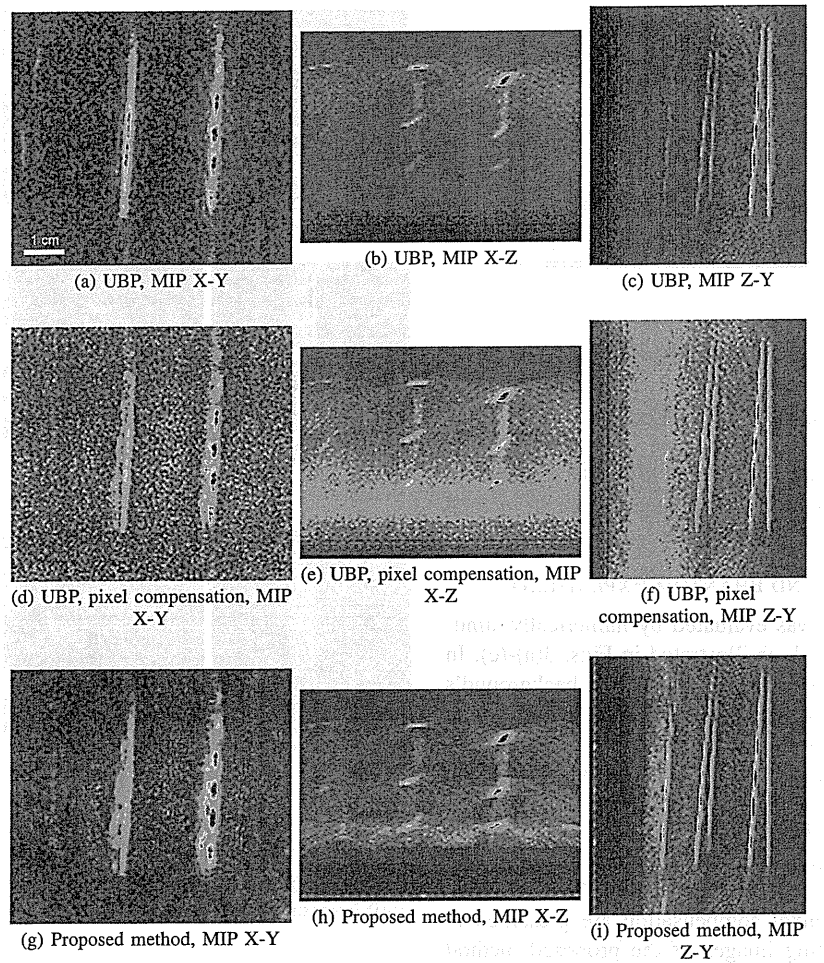

Fig. 4. Reconstructed images by UBP method, conventional depth compensation method, and proposed method. (a)-(c) Reconstructed by UBP method without depth compensation. (d)-(f) Reconstructed by UBP method with conventional depth compensation. (g)-(i) Reconstructed by proposed method.

IV. Conclusion

The simulation and experiment results indicate that the proposed method can greatly reduce side lobes and artifacts compared with the conventional quantitative PAT reconstruction method. We expect that the capability of increasing imaging depth will broaden clinical applications of PAT.

References

[1] C. Li and L.V. Wang, "Photoacoustic tomography and sensing in biomedicine," *Phys. Med. Biol.*, vol. 54, pp. R59-R97, Sep. 2009.

[2] M. Xu and L.V. Wang, "Photoacoustic imaging in biomedicine," *Review of Scientific Instruments*, vol. 77, p.041101, 2006.

[3] B. T. Cox, S. R. Arridge, K. P. Kostli, and P. C. Beard, "Two-dimensional quantitative photoacoustic image reconstruction of absorption distribution in scattering media by use of a simple iterative method," *Applied Optics*, vol. 45, no. 8, Mar. 2006.

[4] M. Xu and L.V. Wang, "Universal back-projection algorithm for photoacoustic computed tomography," *Physical Review E*, vol. 71, 016706, 2005.

[5] M. Xu, Y. Xu, and L.V. Wang, "Time-domain reconstruction algorithms and numerical simulation for thermoacoustic tomography in various geometries," *IEEE. Trans. Bio. Eng.*, vol. 50, no. 9, pp. 1086-1099, Sep. 2003.

[6] G. Paltauf, J.A. Viator, S.A. Prahl, and S.L. Jacques, "Iterative reconstruction algorithm for optoacoustic imaging," *J. Acoust. Soc. Am.*, vol. 112, no. 4, Oct. 2002.

[7] J. Zhang, M.A. Anastasio, P.J.L. Riviere, and L.V. Wang, "Effects of different imaging models on least-squares image reconstruction accuracy in photoacoustic tomography," *IEEE. Trans. Med. Imag.*, vol. 28, no. 11, Nov. 2009.

[8] S. Ma, S. Yang, and H. Guo, "Limited-view photoacoustic imaging based on linear-array detection and filtered mean-backprojection-iterative reconstruction," *J. Appl. Phy.* vol. 106, 123104, 2009.

[9] E. F. D. Azevedo, M. R. Fahey, and R. T. Mills, "Vectorized sparse matrix multiply for compressed row storage format," *Computational Science - ICCS 2005*, vol. 3514, pp. 99-106, 2005.

[10] M. R. Hestenes and E. Stiefel, "Methods of conjugate gradients for solving linear systems," *Journal of Research of the National Bureau of Standards*, vol. 49, no. 6, Dec. pp. 409-436, 1952.

[11] B. T. Cox and P. C. Beard, "Fast calculation of pulsed photoacoustic fields in fluids using k-space methods," *J. Acoust. Soc. Am.*, vol. 117, no. 6, Jun. 2005.

10.1109/ULTSYM.2010.0541

Dual illumination mode photoacoustic tomography for quantitative imaging

K. Fukutani[1], T. Miyasato[1], T. Nakajima[1], Y. Someda[1], Y. Asao[1,3], T. Yagi[1], M. Yamakawa[2], and T. Shiina[3]
[1]Medical Imaging Project, Corporate R&D Headquarters, Canon Inc., Tokyo, Japan
[2]Advanced Biomedical Engineering Research Unit, Kyoto University, Kyoto, Japan
[3]Graduate School of Medicine, Kyoto University, Kyoto, Japan

Abstract—**This study presents an algorithm to estimate the background optical properties for quantitative imaging, based on the initial pressure distribution obtained from photoacoustic tomography (PAT). The algorithm utilizes an alternative illumination mode of our original PAT system, which separately illuminates tissue from forward and backward directions toward an array transducer. The optical properties are determined by minimizing the difference between the following two ratios: one is the ratio of initial pressure distribution obtained from the illumination modes, the other is the ratio of the calculated light fluence distribution. We show that the algorithm estimates the background optical properties even if the initial pressure distribution is reconstructed under the limited-view conditions.**

Keywords; photoacoustic imaging; quantitative imaging; photoacoustic tomography; limited-view; algorithm; deep tissue imaging; effective attenuation coefficient

I. INTRODUCTION

Breast cancer is the second leading cause of cancer deaths in women after lung cancer and is the most common cancer among women [1]. The generally used modalities for breast cancer diagnosis, such as ultrasonography and x-ray mammography, have some limitations including poor contrast and dense glandular tissue imaging. Meanwhile, photoacoustic imaging (PAI) is a promising imaging modality, which can visualize biological tissues with high contrast and high spatial resolution. In PAI, the contrast derived from optical absorption is related to physiological properties such as angiogenesis and tissue oxygen consumption. Therefore, PAI has been used to diagnose breast cancer [2,3]. PAI may overcome the limitations of the generally used modalities, however, deep tissue imaging remains difficult due to strong light scattering in biological tissues. In order to detect signals from deep tissues, we have developed a new photoacoustic tomography (PAT) system, the "dual illumination mode PAT system." For achieving deep tissue imaging, the PAT system alternatively or simultaneously illuminates tissues from a forward and backward direction toward an array transducer. This geometry of illumination makes deep tissue imaging possible in terms of light. Thus, the system visualizes all the absorbers embedded in a 50-mm-thick tissue-mimicking phantom [4].

On the other hand, quantitative PAI for recovering the absorption coefficient distribution is a key issue for estimating blood oxygenation distribution [5]. Estimation of the blood oxygenation level impacts the barest cancer diagnosis since it is closely related to hypermetabolism. Meanwhile, quantitative imaging is quite challenging. The initial pressure distribution reconstructed by PAT is proportional to both the absorption coefficient and the unknown optical fluence distribution. This indicates that recovering the absorption coefficient distribution requires the estimation of the optical fluence, which is a function of the optical properties in the medium. Therefore, if the optical properties of the biological tissue are known, the local optical fluence at all absorber locations can be estimated by applying an appropriate light transport model. Recently, Ranasinghesagara *et al.* developed a reflection-mode photoacoustic technique to obtain the background optical properties of biological tissues [6]. However, the method is not suitable for the PAT system using unfocused transducers.

In this study, we propose an algorithm for estimating the optical properties of a background medium with our developed dual illumination mode PAT system. In contrast to other algorithms for quantitative imaging based on a full-view reconstruction [7,8], this method can minimize the effect of limited-view reconstruction because it makes use of the ratio of reconstructed images.

II. ALGORITHM

The algorithm is based on an alternative illumination mode in our PAT system, which separately illuminates tissue from a forward and backward direction toward an array transducer. From photoacoustic (PA) signal measurements using a short laser pulse, PAT can provide an initial pressure distribution. The initial pressure is a product of the local Grüneisen coefficient, the optical absorption coefficient of the absorbing structures, and the local optical fluence. The local optical fluence at the absorbing structures is assumed to be determined by the background optical properties of a turbid medium such as the anisotropy, scattering coefficient, and absorption coefficients for this study. This assumption is reasonable when the volume of absorbing structures is relatively small compared with that of the background media. Therefore, if the overall anisotropy and the scattering and absorption coefficients of the background medium are held constant, the initial pressure distribution (P_0) at the absorber location r is written by

$$P_0(r) = \Gamma(r) \cdot \mu_a(r) \cdot \Phi(r, \mu_a^b, \mu_s^b, g^b), \quad (1)$$

where $\Gamma(r)$, $\mu_a(r)$, μ_a^b, μ_s^b, g^b, and $\Phi(r)$ are the local Grüneisen coefficient, absorption coefficient of the absorbing structure, background optical absorption coefficient, background optical scattering coefficient, background anisotropy, and local optical fluence, respectively.

In the alternative illumination mode of our PAT system, the initial pressure distribution reconstructed from the forward and backward illumination ($P_0^{forward}$ and $P_0^{backward}$) can be obtained. Let us take a ratio of the initial pressure distribution reconstructed from both illumination modes. Then, the ratio is given by

$$\frac{P_0^{forward}(r)}{P_0^{backward}(r)} = \frac{\Gamma(r)\cdot\mu_a(r)\cdot\Phi^{forward}(r,\mu_a^b,\mu_s^b,g)}{\Gamma(r)\cdot\mu_a(r)\cdot\Phi^{backward}(r,\mu_a^b,\mu_s^b,g)}. \quad (2)$$

On the right-hand side of Eq. (2), $\Gamma(r)$ and $\mu_a(r)$ are canceled. Therefore, the left-hand side of the equation becomes equal to the ratio of the local optical fluence at each illumination mode. Furthermore, the effect of the limited-view problem can be minimized by taking a ratio of the reconstructed data since an absolute value of the initial pressure is not required.

For homogeneous turbid medium, the time independent diffusion equation of optical transport can be written by

$$\mu_a^b\cdot\Phi(r) - D\nabla^2\Phi(r) = S(r), \quad (3)$$

where D, and $S(r)$ are diffusion coefficient and optical source, respectively. The constant D is given by $D = 1/3(\mu_a^b + \mu_s'^b)$, where $\mu_s'^b$ is a reduced scattering coefficient of the background medium. For the diffusion theory, the reduced scattering coefficient $\mu_s'^b$ is defined as $\mu_s'^b = \mu_s^b(1 - g^b)$. This means that the local optical fluence depends only on μ_a^b and $\mu_s'^b$ in the background medium, not on μ_s^b and g^b separately. In deep tissue imaging, the diffusion approximation is valid because the absorbing structures of interest are away from the tissue surface, normally at a depth exceeding several millimeters. Equation (3) can be solved by finite-element method (FEM) at any turbid medium and any sample illumination. Thus, the right-hand side of Eq. (2) can be estimated by forward model simulation based on Eq. (3).

The above discussion indicated that the optical properties of a background medium could be determined by minimizing the difference between the ratio of the initial pressure distribution obtained from the different illumination modes and the theoretically calculated optical fluence ratio. In this study, we choose the objective function (E) as follows:

$$E = \sum_r \sqrt{\left[\frac{P_0^{forward}(r)}{P_0^{backward}(r)} - \frac{\Phi_{Sim}^{forward}(r,\mu_a^b,\mu_s'^b)}{\Phi_{Sim}^{backward}(r,\mu_a^b,\mu_s'^b)}\right]^2}. \quad (4)$$

Consequently, μ_a^b and $\mu_s'^b$ can be estimated by minimizing E. In this minimization, μ_a^b and $\mu_s'^b$ are iteratively updated using a Nelder-Mead simplex-based search, implemented in MATLAB® until E is smaller than a certain value. By making use of this algorithm, the mean optical absorption and mean optical reduced scattering coefficient of the background medium could be quantitatively estimated.

III. NUMERICAL RESULTS

In this section, a numerical simulation is demonstrated to validate the proposed algorithm by estimating the background optical properties from the simulated initial pressure distributions obtained from forward and backward illumination. A three-dimensional example of an absorption coefficient distribution, which consists of three spherical absorbers with absorption coefficients of 1.0 mm^{-1}, is shown in Fig. 1(a). The background absorption coefficient except for absorbing structures and reduced scattering coefficients are constant, with μ_a^b = 0.01 mm^{-1} and $\mu_s'^b$ = 1.0 mm^{-1}. These values yield an effective attenuation coefficient (μ_{eff}^b), defined by $\mu_{eff}^b = (3\mu_a^b(\mu_a^b + \mu_s'^b))^{1/2}$, equal to 0.174 mm^{-1}. The overall simulated dimensions and the diameter of the spherical absorbers are 30×30×30 mm and 2 mm, respectively. Since the grid size was set to 1 mm in each direction, the numerical calculations were performed on a 30×30×30 grid. A 2D array transducer contacted with a side of the background medium (z = 0 mm) is assumed for this study. The array detects PA signals only at this position, leading to limited-view conditions. The array consists of 30×30 detectors with a size of 1×1 mm^2. Optical illumination is given from forward (z = 30 mm) and backward directions (z = 0 mm) against the 2D array transducer. The optical illumination profiles and basic system configuration follow our developed PAT system as shown in the next section.

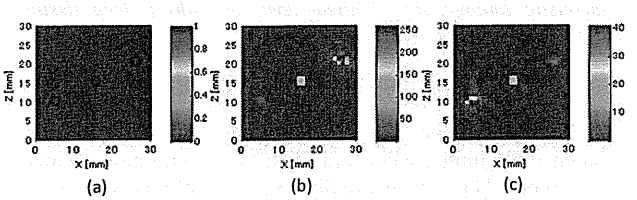

Figure 1. Images of (a) the absorption coefficient distribution, and the reconstructed initial pressure distribution obtained from (b) forward and (c) backward illumination.

The initial pressure distribution from the forward and backward illumination was reconstructed from the simulated PA signals, as shown in Fig. 1(b) and (c). In the PA simulation, the PA signals detected by the array transducer were calculated by solving the PA wave equation, and the simulated PA signals were used to reconstruct images by back-projection algorithm [9]. By using the obtained initial pressure distribution, μ_a^b and $\mu_s'^b$ were estimated by the proposed algorithm. In the minimization of E in Eq. (4), the ratio of the optical fluence from both illumination modes is calculated by FEM at each iteration. Figure 2 shows the convergence of E, μ_a^b, $\mu_s'^b$ and μ_{eff}^b against the iteration number. These results show that the optical properties almost converged to true values as the number of iterations increased, despite the limited-view reconstruction. The values of μ_a^b, $\mu_s'^b$ and μ_{eff}^b at 200 iterations are 0.104, 1.01 and 0.179 mm^{-1}, respectively. The errors remain below 4 %. The main reason for the errors is due to the appearance of artifacts in the reconstructed images. The artifacts then produce local changes in the initial pressure values, providing an error of $P_0^{forward}(r)/P_0^{backward}(r)$ at some absorber locations.

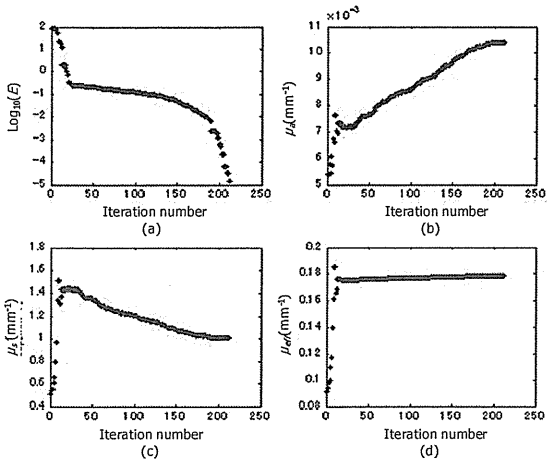

Figure 2. Convergence of (a) a log of the object function, (b) the absorption coefficient, (c) the reduced scattering coefficient and (d) the effective attenuation coefficient as a function of iteration in the case of numerical study.

IV. EXPERIMENTAL RESULTS

To confirm the utility of the algorithm with experimental studies, the PA signals were measured by our developed PAT system. Figure 3(a) shows a schematic diagram of the dual illumination mode PAT system. In this system, a tissue-mimicking phantom is held by two parallel plates. In alternative illumination modes, the phantom is illuminated separately from a forward and backward direction toward an array transducer. The optical intensity profiles on the phantom surface from forward and backward illumination are shown in Fig. 3(b) and (c), respectively. A 2D rectangular 345-element (15×23) transducer with element size of 2×2 mm^2 is selected. The shape of the transducer allows direct illumination of tissue surfaces in front of the array transducer through a 10-mm-thick holding plate, which can maximize the optical fluence in the imaging area. The transducer frequency is designed for 1 MHz to receive deep PA signals with minimal ultrasonic attenuation. A Ti-sapphire optically pumped with a Q-switched Nd:YAG laser, which can tune a wavelength from 750 to 850 nm, has been integrated for deep light penetration in biological tissue. The laser beam is sufficiently broadened to satisfy the maximum permissible exposure limit. The PA signals are collected at each illumination mode, and the initial pressure distribution was reconstructed from the obtained signals by using a back-projection algorithm.

The base of the tissue-mimicking phantom with a size of 80(x)×80(y)×50(z) mm was made with water (450 mL), agar powder (7.5 g) and Intralipid® 10% (50 mL). The absorption and reduced scattering coefficients of the base phantom were 0.0005 mm^{-1} and 0.31 mm^{-1} at 797 nm, respectively. These values yield an effective attenuation coefficient equal to 0.0216 mm^{-1}. To obtain the optical properties of the background medium, a single 0.3 mm rubber wire embedded at a depth of 25 mm below the surface of the base phantom was imaged at different illumination modes. The array transducer contacted with a side of the holding plate detects the PA signals through the plate, as shown in Fig. 3(a). The laser beam was illuminated from the top and bottom surface of the phantom, through the plate. The reconstructed volume was 30(x)×46(y)×48(z) mm, which is the same volume as the size of the array transducer multiplied by the thickness of the compressed phantom. Figure 4 shows the initial pressure distribution reconstructed from the forward and backward illumination modes.

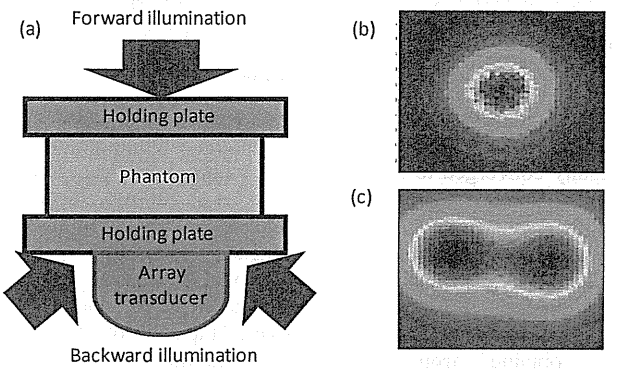

Figure 3. (a) Schematic diagram of the dual illumination mode PAT system. Optical intensity profiles of (b) forward and (c) backward illumination.

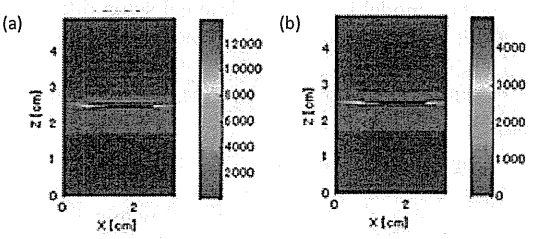

Figure 4. The reconstructed initial pressure distribution obtained from (a) forward and (b) backward illumination.

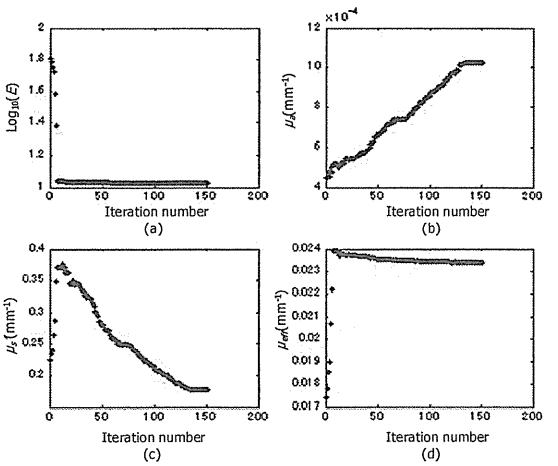

Figure 5. Convergence of (a) a log of the object function, (b) the absorption coefficient, (c) the reduced scattering coefficient and (d) the effective attenuation coefficient as a function of iteration in the case of the phantom study using our PAT system.

By using the ratio of the initial pressure distribution, μ_a^b, $\mu_s'^b$, and μ_{eff}^b were estimated by minimizing E. Figure 5 shows the convergence of E, μ_a^b, $\mu_s'^b$, and μ_{eff}^b against the iteration number. The results show that μ_a^b and $\mu_s'^b$ converged to the wrong values. On the other hand, μ_{eff}^b remains almost constant after the number of iterations exceeded 10. The value of μ_{eff}^b at 150 iterations is 0.0234 mm^{-1}, which is almost the same as the true value of 0.0216 mm^{-1}. The error of μ_{eff}^b is 8.3 %.

V. DISCUSSION

Experimental results showed that μ_a^b and $\mu_s'^b$ converged to the wrong values although in the numerical simulation they eventually converged to the true values within 4 % error. The reason for these results is considered to be as follows. In the numerical results shown in Fig. 2(a) and (d), the reduction of E becomes smaller after μ_{eff}^b almost reaches a constant value. From the above result and the forward model simulation of the optical fluence, we found that a combination of μ_a^b and $\mu_s'^b$, yielding a constant μ_{eff}^b, is not sensitive to the ratio of optical fluence obtained from the different illumination modes. Consequently, the convergence of μ_a^b and $\mu_s'^b$ to the true values is strongly affected by the level of noise and artifacts. In addition, our proposed algorithm is highly dependent on the accuracy of calculating the optical fluence distribution. If the light propagation model in the experimental setup differs from theory, it gives an inaccurate optical fluence distribution. Thus, it would be difficult to estimate μ_a^b and $\mu_s'^b$ separately, especially from experimental studies using real tissues such as breast tissue.

Even though considering that our algorithm is robust against noise and artifacts, and the accuracy of the light propagation model, μ_{eff}^b could be estimated within 10 % error from the experimental study. This result is encouraging because μ_{eff}^b is a sufficient parameter for calculating the optical fluence of a background medium in some cases. Our current PAT system detects PA signals at one location. In contrast, the next generation system under development changes the detection position of PA signals by scanning the optical sources and the array transducer. The system configuration makes the optical illumination profiles uniform over a large area because the PA signals detected at the same location are averaged. For an infinitely broad isotropic source in an infinite homogeneous turbid medium, the optical fluence is written by

$$\Phi(z) = \Phi_0 \cdot \exp(-\mu_{eff} \cdot z), \quad (5)$$

where Φ_0 and z are the optical fluence on the sample surface and the depth from the illumination surface, respectively. In the next generation system, the optical illumination can be assumed to be an infinitely broad isotropic source, as discussed above. Therefore, μ_{eff}^b is a unique parameter for estimating the optical fluence in the next generation PAT system. Thus, our proposed algorithm with the next-generation PAT system would be more useful for quantitative imaging in practice.

VI. CONCLUSIONS

We have proposed an algorithm for estimating the mean optical properties of a background medium. The results demonstrated that the proposed algorithm could estimate the optical properties of the background medium by making use of the alternative illumination modes of our PAT system, which separately illuminates tissue from a forward and backward direction toward an array transducer. In contrast to other algorithms, our algorithm works with a limited-view reconstruction since an absolute value of the initial pressure is not required. Furthermore, the algorithm showed robustness against noise and artifacts when used to estimate the effective attenuation coefficient of the background medium. Therefore, the dual illumination mode PAT system would be promising not only for deep tissue imaging but also for quantitative imaging.

ACKNOWLEDGMENT

This work is partly supported by the Innovative Techno-Hub for Integrated Medical Bio-imaging Project of the Special Coordination Funds for Promoting Science and Technology, from the Ministry of Education, Culture, Sports, Science and Technology (MEXT), Japan.

REFERENCES

[1] Breast Cancer Facts & Figures 2009-2010, American Cancer Society, Inc. 2009.

[2] S. Manohar, S. E. Vaarjes, J. C. G. Van Hespen, J. M. Klaase, F. M. Van den Engh, W. Steenbergen, and T. G. van Leeuwen, "Initial results of in vivo non-invasive cancer imaging in the human breast using near-infrared photoacoustics," Opt. Express, vol. 15, no. 19, pp. 12277-12285, September 2007.

[3] A. A. Oraevsky, A. A. Karabutov, S. V. Solomatin, V. Savateeva, V. G. Andreev, Z. Gatalica, H. Singh, and R. D. Leming, "Laser optoacoustic imaging of breast cancer in vivo," Proc. SPIE 4256, pp.6-15, 2001.

[4] K. Fukutani, Y. Someda, M. Taku, Y. Asao, S. Kobayashi, T. Yagi, M. Yamakawa, T. Shiina, T. Sugie, and M. Toi, to be published.

[5] H. F. Zhang, K. Maslov, G. Stoica, and L. V. Wang, "Functional photoacoustic microscopy for high-resolution and noninvasive in vivo imaging," Nat. Biotechnol., no. 21, pp. 803-806, July 2006.

[6] J. C. Ranasinghesagara, Y. Jian, X. Chen, K. Mathewson, and R. J. Zemp, "Photoacoustic technique for assessing optical scattering properties of turbid media," J. Biomed. Opt., vol. 14, 04050, July/August 2009.

[7] B. T. Cox, S. R. Arrige, K. P. Köstli, and P. C. Beard, "Two-dimensional quantitative photoacoustic image reconstruction of absorption distributions in scattering media by use of a simple iterative method," Appl. Opt., vol. 45, no. 8, pp. 1866-1875, March 2006.

[8] B. Banerjee, S. Bagchi, R. M. Vasu, and D. Roy, "Quantitative photoacoustic tomography from boundary pressure measurements: noniterative recovery of optical absorption coefficient from the reconstructed absorbed energy map," J. Opt. Soc. Am. A, vol. 25, no. 9, pp. 2347-2356, September 2008.

[9] M. Xu and L. V. Wang, "Universal back-projection algorithm for photoacoustic computed tomography," Phys. Rev. E vol. 71, 016706, 2005.

J Med Ultrasonics (2010) 37:129–135
DOI 10.1007/s10396-010-0265-8

ORIGINAL ARTICLE

Calculus detection for ultrasonography using decorrelation of forward scattered wave

Hirofumi Taki · Takuya Sakamoto · Makoto Yamakawa · Tsuyoshi Shiina · Toru Sato

Received: 30 September 2009 / Accepted: 25 March 2010 / Published online: 15 May 2010

Abstract
Purpose The purpose of this paper is to propose a novel strategy to detect small calculi efficiently.
Methods The proposed calculus detection strategy focuses on decorrelation of forward scattered waves caused by the failure of Born's approximation. A calculus causes waveform changes of transmit pulses, resulting in a decrease in the cross-correlation coefficients calculated from IQ signals scattered near the calculus position. Therefore, we can detect calculi from the appearance of dips in correlation coefficients.
Results When a calculus exists in a digital tissue map, sharp and deep dips in cross-correlation coefficients between acoustic IQ signals appear around the calculus. By contrast, no apparent dip exists when a tissue map contains no calculus. A scan line interval of 0.2 mm or less is appropriate for the conditions simulated in this paper, and the proper transmit focal range for the proposed method is at a calculus range.
Conclusion These results imply that the proposed strategy can improve the efficiency of US devices for small calculus detection.

H. Taki (✉) · T. Sakamoto · T. Sato
Graduate School of Informatics, Kyoto University,
Yoshida-honmachi, Sakyo-ku, Kyoto 606-8501, Japan
e-mail: hirofumi.taki@mb6.seikyou.ne.jp

M. Yamakawa
Advanced Biomedical Engineering Research Unit,
Kyoto University, Yoshida-honmachi, Sakyo-ku,
Kyoto 606-8501, Japan

T. Shiina
Graduate School of Medicine, Kyoto University,
Yoshida-honmachi, Sakyo-ku, Kyoto 606-8501, Japan

Keywords Calculus detection · Forward scattered wave · Decorrelation · Ultrasonography · CFAR

Introduction

Ultrasonography (US) does not involve exposure to ionizing radiation and has an excellent ability to depict soft tissue, making it a convenient and effective clinical imaging tool. In contrast, US has poor sensitivity for detection of calculi compared with computed tomography (CT). Because the detection of calculi is important to distinguish between malignant masses and benign ones, the use of US is often an adjunct to other diagnostic tests [1–6].

A calculus is usually identified as a high-intensity echo with acoustic shadowing or enhancement [7, 8]. One strategy for detecting calculi is to detect high-intensity echoes in a B-mode image. This problem is equivalent to detecting targets in non-stationary noise and clutter while maintaining a constant probability of a false alarm. Finn et al. [9] designed a cell-averaging constant false alarm rate (CA CFAR) detector to set an adaptive threshold according to local noise levels. Hansen et al. [10] proposed a cell-averaging logarithmic constant false alarm rate (LOG CFAR) detector for operating over a larger dynamic range of background noise levels than the CA CFAR detector. To detect targets in an inhomogeneous medium, many researchers have reported several types of CFAR detectors [11, 12]. However, echo intensity from a small calculus is too low to detect it by simply selecting high-intensity echo masses.

Tissue harmonic imaging (THI) suppresses speckle artifacts utilizing harmonics, resulting in the improvement of contrast resolution [1, 13, 14]. THI thus helps to evaluate mass borders; however, it has insufficient calculus

detectability compared with CT. By contrast, spatial compound imaging generates a single B-mode image from multiple sweeps [15, 16]. This technique improves image quality in terms of mass margins and internal architectures at the cost of a decrease in frame rate and suppression of acoustic shadowing [17]. Acoustic shadowing is one of the essential factors to detect small calculi, and thus compound imaging is inappropriate for calculus detection.

In general, US has difficulty depicting small calculi of 3.0 mm or less in size [2]. In addition, US depends heavily on operator skill. Conventional methods such as CFAR only provide information on backscattered waves from the ROI, and thus would theoretically hardly ever detect a small calculus when a high-echo target such as a layered structure exists close to the calculus. In this paper, we propose a calculus detection method employing the novel strategy to focus on decorrelation of forward scattered waves caused by the failure of Born's approximation. Since the proposed method detects a calculus using decorrelation of forward scattered waves, there is a good probability of detecting a small calculus from the waveform change in transmit waves caused by the calculus when the echo intensity of the calculus is too low to be detected by CFAR.

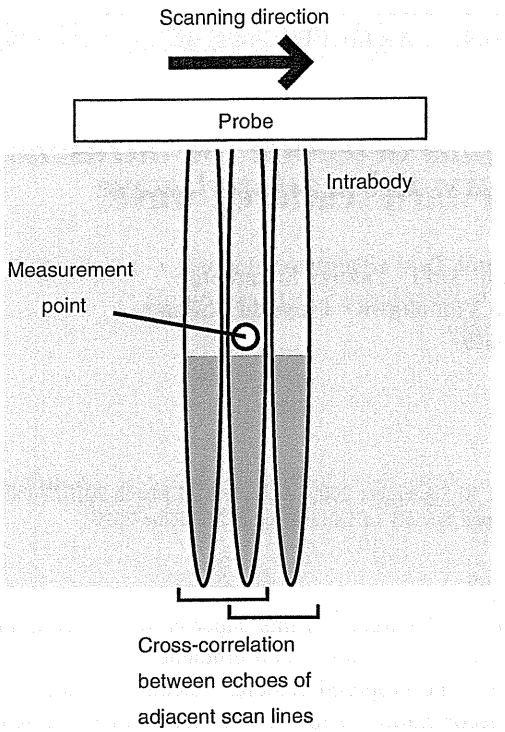

Fig. 1 Schema of the proposed calculus detection method using cross-correlation coefficients between two IQ signals of adjacent scan lines

Materials and methods

Calculus detection using decorrelation of forward scattered waves

The proposed calculus detection strategy focuses on decorrelation of forward scattered waves caused by the failure of Born's approximation. For the investigation of decorrelation of forward scattered waves, we employed the cross-correlation between acoustic IQ signals of adjacent scan lines. Figure 1 shows the schema of this process. The cross-correlation coefficient behind a measurement point is

$$c(i,j) = \max_{l} g(i,j,l), \tag{1}$$

$$g(i,j,l) = \left| \sum_{J=j}^{j+L_w} e(i,J)e^*(i+1,J+l) \right| \Big/ \sqrt{p(i,j)p(i+1,j+l)}, \tag{2}$$

$$p(i,j) = \sum_{J=j}^{j+L_w} e(i,J)e^*(i,J), \tag{3}$$

where $e(i, j)$ is the IQ datum at E_{ij}, a pixel in a B-mode image, L_w is the correlation window width, and i and j are, respectively, the lateral and range coordinates in a B-mode image. When the medium is homogeneous and the layered structure is parallel to the skin surface, the maximization of $g(i, j, l)$ is not needed. We introduced the parameter l to suppress the path length difference between adjacent scan lines caused by the sound velocity variation in the medium and by the slope of a layered structure. In this study, two correlation windows were set with the depth ranges of 12.5–17.5 and 17.5–22.5 mm. When a small calculus exists in an acoustic beam, the waveform of a transmit wave changes because of several causes: creeping waves, a fast wave that goes through the calculus, diffraction, and multiple reflections in the calculus. Therefore, the echo waveform of a scan line with a calculus, returned from the inhomogeneous medium behind the calculus, was quite different from that without a calculus, as shown in Fig. 2. We can presume the existence of a calculus from the waveform difference between echoes of adjacent scan lines by calculating cross-correlation coefficients.

To equalize the influence of the noise among all cases with different simulation parameters, we calculated the average μ and standard deviation σ of cross-correlation coefficients by echoes scattered from positions more than 1 mm apart from the center, and then normalized the correlation coefficients using the averages and standard deviations.

Computer simulation with FDTD method

To evaluate the efficiency of the proposed calculus detection method, we employed PZFlex, a computer simulation

tool based on a finite-difference time-domain (FDTD) method [18, 19]. Here we set the grid size to 0.02 mm, satisfying the operating condition of PZFlex. In this simulation, a 19.1-mm-wide linear array probe was utilized. The probe had 32 elements, 0.5 mm wide, and an element gap of 0.1 mm. The center frequency of the transmit pulse was 4 MHz with a 60% fractional bandwidth.

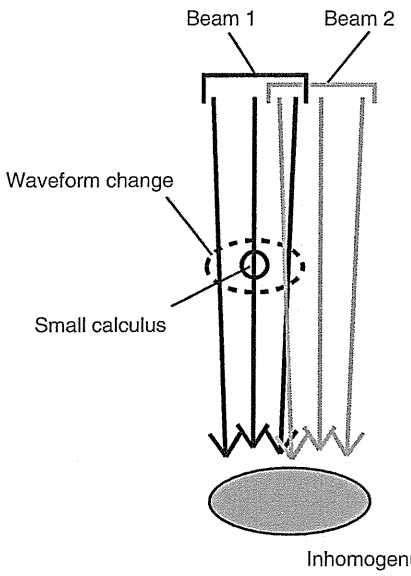

Fig. 2 Waveform change of a transmit pulse that originated from a calculus

Modification of input intensity for beamforming

To form a narrower scan line interval than the element interval, the input intensity of both edges of the activated elements are modified. As shown in Fig. 3, the amplitudes of transmit waves from both edge elements are controlled to correspond to the transmit beam position. When the center of the transmit beam is at the center of an element gap, 16 elements are activated, and all transmit pulses have the same amplitude. Otherwise, 17 elements are activated, and the amplitude of two transmit pulses radiated from both edge elements are modified, as shown in Fig. 3. At the transmit event, we employed four foci, fixed foci at 1, 1.5, and 2 cm depth, and dynamic focusing. By contrast, we utilized dynamic focusing at receive events with the same modification process.

Digital tissue map

To investigate the efficiency of the proposed calculus detection strategy, we prepared five simulated digital tissue maps with a calculus and five without a calculus. Figure 4 shows a digital tissue map with a calculus. The muscle layer, containing 5% minute fat droplets 0.1 mm in size, is located under skin that is 2 mm thick. A 0.5-mm-diameter calculus or a 1-mm-thick, 4-mm-wide connective tissue mass is embedded at the center at a depth of 10 mm, and a 1-mm-thick connective tissue layer is set at a depth of 15 mm.

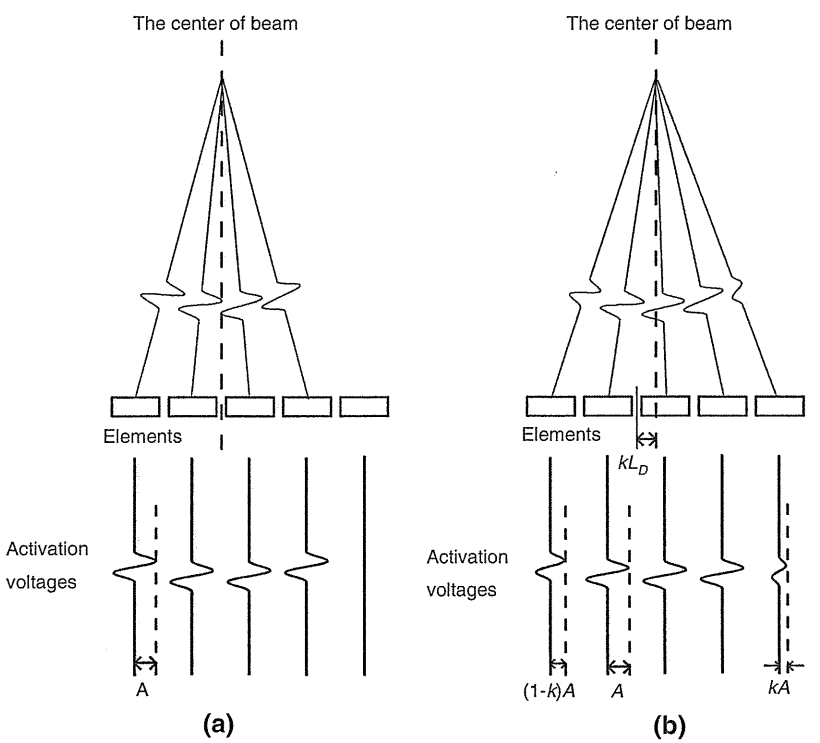

Fig. 3 Schema of modification of input intensity for beamforming. **a** When a scan line is set at the center of an element gap, all activated elements radiate pulses with the same amplitude, where A denotes the amplitude. **b** When a distance exists between a scan line and the center of an element gap, the amplitudes of two pulses radiated from elements at both edges are modified to correspond to the distance, where L_D is the element interval and k is a real number satisfying $0 < k < 1$

Statistical analysis

We performed statistical analyses to compare two groups in terms of the dip depth of correlation coefficients using Student's t test.

Results

To survey the proper scan line interval and transmit the focal range for the proposed method, we examined the cross-correlation coefficients between the acoustic IQ signals of five digital tissue maps with a small calculus. Scan line intervals of 0.1, 0.2, 0.3, and 0.6 mm were used with the transmit focus fixed at 10, 15, and 20 mm and dynamically changed. Figure 5 shows the cross-correlation coefficients obtained using a digital tissue map with a calculus. In all cases, dips of correlation coefficients appear around the center, i.e., the position of the calculus. These results indicate that the waveform changes of transmit pulses, which originate from a calculus, suppress correlation coefficients around the center. When the center of a correlation window was 15 mm deep, i.e., a correlation window with a layered structure, deeper dips appeared as compared with those when the center was 20 mm, where the level of significance for Student's t test is 0.005. Since the influence of noise among all cases with different simulation parameters was equalized by the normalization process using averages and standard deviation, we investigated proper parameters for the proposed calculus detection method using the minimum number of normalized correlation coefficients where their lateral positions are within 1 mm of the center.

Figure 6 shows the averages and standard deviations of dip depth of correlation coefficients around the center among five digital maps. When the transmit focal range was fixed at a depth of 10 mm, there was no statistical significance concerning the dips of correlation coefficients between scan line intervals of 0.1 and 0.2 mm, as shown in Fig. 6a. By contrast, when the center of the correlation window was 15 mm, dips of 0.3- and 0.6-mm scan line intervals were shallower than that of 0.1-mm scan line intervals, where the levels of significance for Student's t

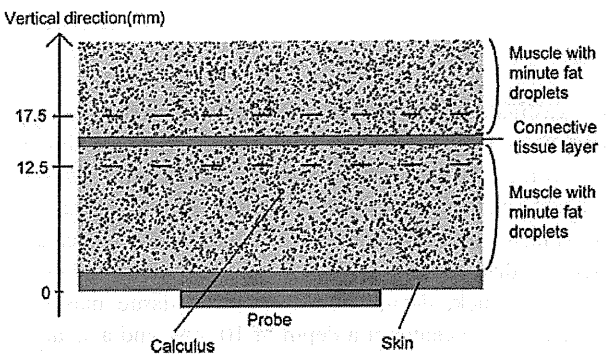

Fig. 4 Digital tissue map with a calculus

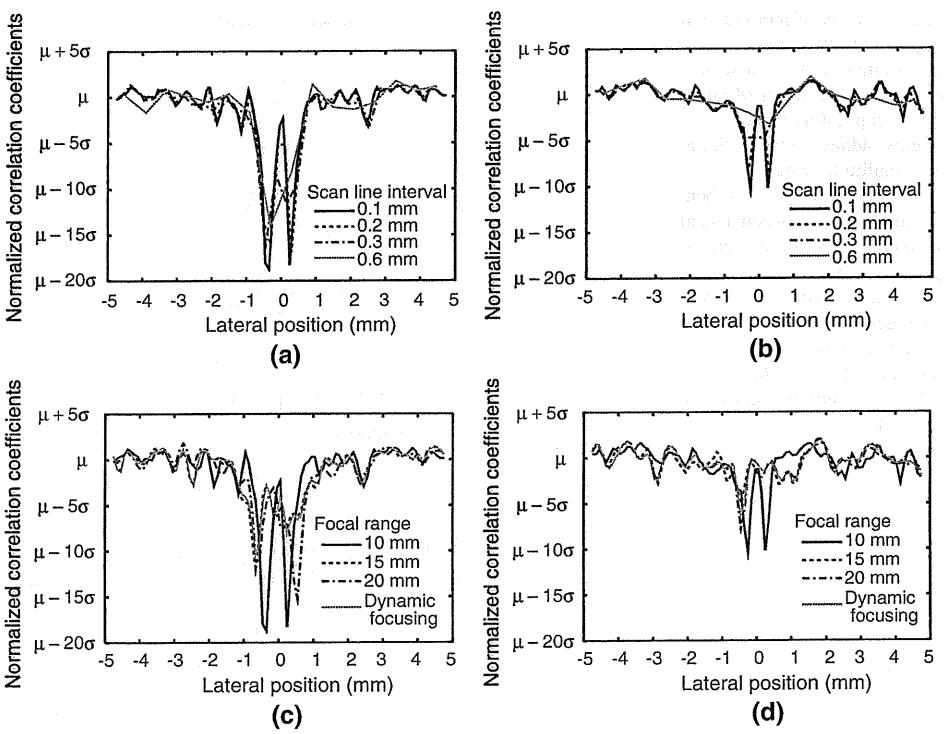

Fig. 5 Cross-correlation coefficients between two IQ signals of adjacent scan lines. **a** Comparison of correlation coefficients with respect to scan line intervals when the center of correlation windows are 15 mm and **b** 20 mm, where the transmit focal range is 10 mm. **c** Comparison of correlation coefficients with respect to transmit focal ranges when the center of correlation windows are 15 mm and **d** 20 mm, where the scan line interval is 0.1 mm

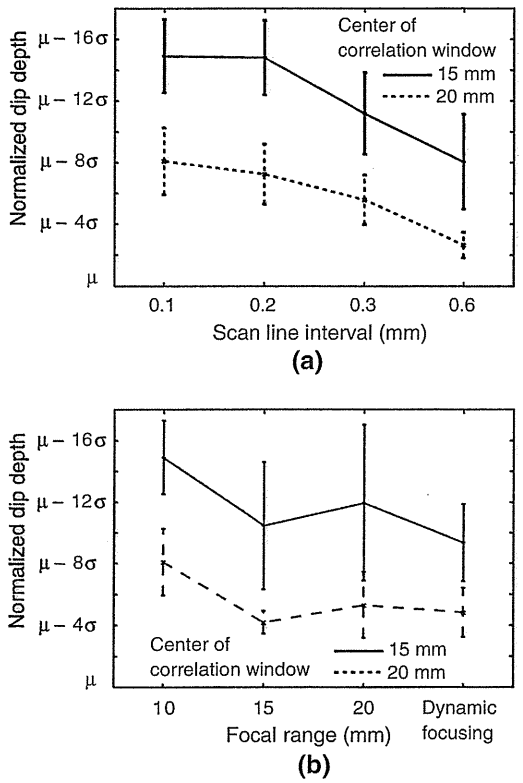

Fig. 6 Averages and standard deviations of dip depth of correlation coefficients around the calculus position. **a** Comparison of dip depth with respect to scan line intervals, where the transmit focal range is 10 mm. **b** Comparison of dip depth with respect to transmit focal ranges, where the scan line interval is 0.1 mm

tests are 0.05 and 0.005, respectively. As shown in Fig. 6b, when the scan line interval was 0.1 mm, a transmit beam with a fixed focal range of 10 mm, the calculus depth, resulted in the deepest dips of correlation coefficients with and without an echo from a layered structure in the signal cut out by a correlation window. In particular, the dynamic focusing for transmit beams deteriorated the conspicuousness of correlation dips. These results show that the proper scan line interval is 0.2 mm or less, and the focal range should be at the calculus depth.

A specular echo from a flat structure often interferes with the detection of a calculus in an US test. To confirm the ability of the proposed method to distinguish a calculus from a flat structure, we compared correlation coefficients of a digital tissue map with a calculus and that with a flat connective tissue mass. Figure 7 shows that dips of correlation coefficients appear only when a digital tissue map with a calculus is used, where the scan line interval is 0.1 mm and the focal range is set at 10 mm, the calculus depth. These results indicate the capability of the proposed method to detect a calculus in an inhomogeneous human body with several specular echoes.

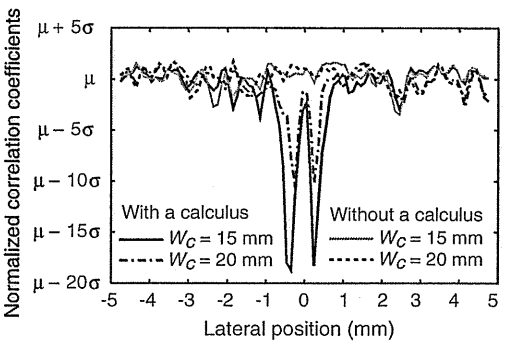

Fig. 7 Correlation coefficients of digital maps with and without a calculus. Dips of correlation coefficients appear only when there is a calculus, where W_c denotes the center of correlation windows

Discussion

In this study, we proposed a calculus detection method focusing on decorrelation of forward scattered waves caused by the failure of Born's approximation. We investigated the ability of the method by using a computer simulation, and optimized the scan line interval and the focal range of transmit beams. This study verified that a calculus creates dips in cross-correlation coefficients around the center; by contrast, a flat connective tissue mass does not. This result indicates that the proposed method has the capability to detect a small calculus 0.5 mm wide in an inhomogeneous human body.

A wide scan line interval decreases the overlap between two beams of adjacent scan lines, suppressing the correlation coefficients between IQ signals of adjacent scan lines. This conceals the decrease in correlation coefficients originating from a calculus. By contrast, when a scan line interval is sufficiently narrow to raise correlation coefficients of adjacent scan lines without a calculus to 1, a calculus creates dips in correlation coefficients, and the proposed method can then detect the calculus effectively. Therefore, for the proposed method a scan line interval should have an upper limit. Under the conditions simulated in this paper, the limit was about 0.2 mm.

When a scan line interval was sufficiently narrow, a calculus influenced multiple transmit beams, resulting in high cross-correlation coefficients located close to the calculus, as shown in Fig. 8. By contrast, when a transmit beam encountered a calculus, a correlation coefficient was calculated from two IQ signals with and without the waveform change caused by the calculus, creating a dip in correlation coefficients. Therefore, two dips in correlation coefficients appeared in cases where the scan line intervals were 0.1 and 0.2 mm. As shown in Fig. 9, a narrow beam at a calculus depth increases the waveform change of the beam caused by a calculus, resulting in deep dips in

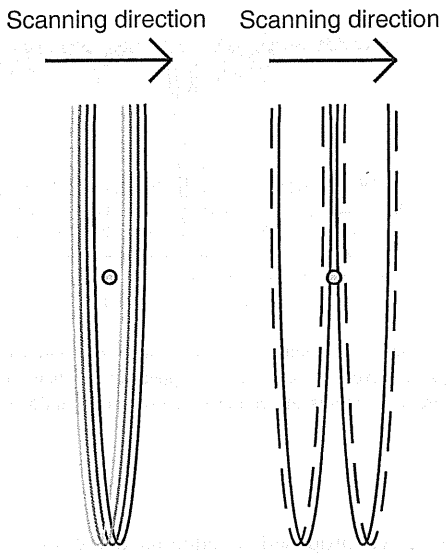

Fig. 8 Appearance of two dips of correlation coefficients calculated using a digital tissue map with a calculus. **a** When scan lines are located close to a calculus, waveform changes originating from the calculus occur in all the pulses of the scan lines. Therefore, the echoes of adjacent scan lines are similar in waveform, resulting in high correlation coefficients at the position close to the calculus. **b** When a transmit beam comes into contacts with a calculus, two IQ signals with and without a calculus in the beams adjoin, creating a dip in correlation coefficients

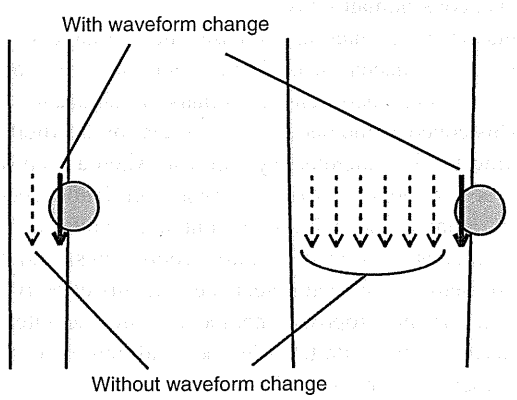

Fig. 9 Schema of waveform change that originated from a calculus comparing a narrow and wide transmit beam

correlation coefficients. Thus, the proper focal range for the proposed method is at calculus depth.

This paper described only the results of a simulation study and did not include any in vitro or in vivo data. There are several major hurdles that have to be overcome before clinical application of this technology.

In conclusion, we proposed a novel calculus detection method focusing on decorrelation of forward scattered waves caused by the failure of Born's approximation, verified the efficacy of the method via computer simulation, and investigated a proper transmit focal range and scan line interval. The results imply the capability of the method to detect small calculi 0.5 mm in diameter in an inhomogeneous human body.

Acknowledgments This work was partly supported by the Research and Development Committee Program of the Japan Society of Ultrasonics in Medicine and the Innovative Techno-Hub for Integrated Medical Bio-imaging Project of the Special Coordination Funds for Promoting Science and Technology from the Ministry of Education, Culture, Sports, Science and Technology (MEXT), Japan.

References

1. Özdemir H, Demir MK, Temizöz O, et al. Phase inversion harmonic imaging improves assessment of renal calculi: a comparison with fundamental gray-scale sonography. J Clin Ultrasound. 2008;36:16–9.
2. Fowler KAB, Locken JA, Duchesne JH, et al. US for detecting renal calculi with nonenhanced CT as a reference standard. Radiology. 2002;222:109–13.
3. Lamb PM, Perry NM, Vinnicombe SJ, et al. Correlation between ultrasound characteristics, mammographic findings and histological grade in patients with invasive ductal carcinoma of the breast. Clin Radiol. 2000;55:40–4.
4. Jacob D, Brombart JC, Muller C, et al. Analysis of the results of 137 subclinical breast lesions excisions. Value of ultrasonography in the early diagnosis of breast cancer. J Gynecol Obstet Biol Reprod (Paris). 1997;26:27–31.
5. Mahnken AH, Mühlenbruch G, Das M, et al. MDCT detection of mitral valve calcification: prevalence and clinical relevance compared with echocardiography. Am J Roentgenol. 2007;188:1264–9.
6. Liu F, Coursey CA, Grahame-Clarke C, et al. Aortic valve calcification as an incidental finding at CT of the elderly: severity and location as predictors of aortic stenosis. Am J Roentgenol. 2006;186:342–9.
7. Janetschek G, Putz A, Feichtinger H. Renal transitional cell carcinoma mimicking stone echoes. J Ultrasound Med. 1988;7:83–6.
8. Roesel GC, Toepfer NJ, Battino BS, et al. A calcified papillary renal cell carcinoma masquerading as a renal pelvic calculus. Curr Urol. 2007;1:217–8.
9. Finn HM, Johnson RS. Adaptive detection mode with threshold control as a function of spatially sampled clutter-level estimates. RCA Rev. 1968;29:414–65.
10. Hansen VG, Ward HR. Detection performance of the cell averaging LOG/CFAR receiver. IEEE Trans Aerosp Electron Syst. 1972;5:648–52.
11. Zhu Y, Weight JP. Ultrasonic nondestructive evaluation of highly scattering materials using adaptive filtering and detection. IEEE Trans Ultrason Ferroelect Freq Control. 1994;41:26–33.
12. Kamiyama N, Okamura Y, Kakee A, et al. Investigation of ultrasound image processing to improve perceptibility of microcalcifications. J Med Ultrasonics. 2008;35:97–105.
13. Schmidt T, Hohl C, Haage P, et al. Diagnostic accuracy of phase-inversion tissue harmonic imaging versus fundamental B-mode sonography in the evaluation of focal lesions of the kidney. Am J Roentgenol. 2003;180:1639–47.
14. Rosen EL, Soo MS. Tissue harmonic imaging sonography of breast lesions improved margin analysis, conspicuity, and image